

Synthesis, Characterization, and Stability of Fe–MCM-41 for Production of Carbon Nanotubes by Acetylene Pyrolysis

Placidus B. Amama, Sangyun Lim, Dragos Ciuparu, Yanhui Yang, Lisa Pfefferle, and Gary L. Haller*

Department of Chemical Engineering, Yale University, 9 Hillhouse Ave., New Haven, Connecticut 06520

Received: June 29, 2004; In Final Form: November 18, 2004

Fe-substituted MCM-41 molecular sieves with ca. 1, 2, and 3 wt % Fe were synthesized hydrothermally using different sources of colloidal silica (HiSil and Cab-O-Sil) and characterized by ICP, XRD, N₂ physisorption, UV–vis, EPR, TPR, and X-ray absorption. Catalysts synthesized from Cab-O-Sil showed higher structural order and stability than those from HiSil. The local environment of Fe in the mesoporous material as studied by UV–vis reveals the dominance of framework Fe in all the as-synthesized Fe–MCM-41 samples. Dislodgement of some Fe species to extraframework location occurs upon calcination, and this effect is more severe for Fe–MCM-41 (2 wt %) and Fe–MCM-41 (3 wt %), as confirmed by EPR and X-ray absorption. These materials have been used as catalytic templates for the production of carbon nanotubes (CNTs) by acetylene pyrolysis at atmospheric pressure. A relationship between the Fe loading in MCM-41 and the carbon species produced during this reaction has been established. Using our optimized conditions for this system, Fe–MCM-41 with ca. 2 wt % Fe showed the best results with particularly high selectivity for single-wall carbon nanotube (SWNT) production. This catalyst was selective for carbon nanotubes with a low amount of amorphous carbon for a narrow range of temperatures from 1073 to 1123 K. To account for the different selectivity of these catalysts for CNTs production, the local environment and chemical state of Fe in the used catalyst was further probed by X-band EPR.

1. Introduction

MCM-41 and related mesoporous molecular sieves of the M41S family are materials of great interest because of their remarkable physical properties such as large surface area (>1000 m²/g) and pore volumes (>0.8 cm³/g), very narrow pore size distribution, and the ease with which their surface can be functionalized.¹ Also, their uniform and tunable pore diameters make them well-adapted as good catalytic supports. Generally, pure silica MCM-41 has limited catalytic activity; active catalytic sites can be generated in MCM-41 by isomorphously substituting silicon with a metal.² Several studies have been dedicated to the investigation of transition-metal-substituted MCM-41 because of their wide range of applications in catalysis. Specifically, Co, Ni, and Fe-substituted MCM-41 are materials of interest to us because these metals are highly active and selective for the production of carbon nanotubes (CNTs).

In previous studies, this laboratory demonstrated the templated growth of SWNT from highly ordered Co-incorporated MCM-41 using the CO disproportionation reaction.^{4,5} The use of mesoporous silica rather than a zeolitic material as a catalytic template for production of CNTs is gaining prominence because of the possibility of controlling the pore diameter independent of the chemical composition of the pore walls. This allows these parameters to be used independently to control the size of the metal particles incorporated in the mesopores from which the initiation of CNT growth is believed to occur. The metal particle plays an important role during CNT production and reports abound showing a direct correlation between the size of the metal nanoparticle and the eventual tube diameter.^{5,6} Thus, the

ultimate goal of being able to control the diameter of CNTs would require a thorough understanding of the microstructure, stability, and chemical properties of the catalytic template.

In comparison to the other traditional metals (Co, Ni) used for CNTs synthesis, Fe has been reported by Hernadi et al.^{7,8} and Dai et al.⁹ to show the highest activity in the decomposition of acetylene. Because hydrocarbon gases are more common, the use of acetylene offers a means of scaling up production of CNTs. Acetylene is considered a good carbon source for single-wall carbon nanotubes (SWNT) production because it contains fewer number of carbon atoms per molecule and greater activity in comparison to other hydrocarbons such as benzene.¹⁰ In reality, several reports^{11–15} reveal that CNTs formed by the pyrolytic decomposition of acetylene over Fe catalysts are usually multiwalled carbon nanotubes (MWNT). This has been widely rationalized to be due to the high reactivity of acetylene. Parallel studies carried out hitherto involved the use of Fe supported on alumina or silica by either sol–gel,^{13,16} adsorption precipitation,¹⁷ or impregnation¹⁸ techniques and have been used mostly in CVD¹⁶ studies. So far, only the work of Duxiao and co-workers¹² has demonstrated the use of Fe-impregnated mesoporous molecular sieve as a catalytic template to produce CNTs via this method. In their study, the stability of the catalytic template and the state of the catalytically active component and the microstructure of the catalyst were not the focus of the work.

Herein, we present a comprehensive characterization of the catalyst carried out by various techniques such as XRD, N₂ physisorption, UV–vis, EPR, TPR, TEM, and X-ray absorption. This is the first study demonstrating the use of MCM-41 with Fe incorporated into the framework of MCM-41 and the first study of CNT growth on Fe catalyst focusing on thorough

* To whom correspondence should be addressed.

characterization of the catalyst. In brief, this study is aimed at investigating the following features of Fe–MCM-41: (i) the effect of Fe amount on the structure and the local environment of Fe species before and after reaction, (ii) the effect of the source of colloidal silica used for the synthesis on the stability and the mesoporous structural integrity, (iii) the effect of Fe amount on the reactivity, and (iv) the relationship between the Fe loading and the selectivity for CNT production.

2. Experimental Section

Synthesis of Catalyst. Fe–MCM-41 was synthesized under hydrothermal conditions adapted from the recipe previously described for V-substituted MCM-41 by Lim and Haller¹⁹ using cetyltrimethylammonium hydroxide (CTMAOH) as the template. CTMAOH was prepared by the ion-exchange of 20 wt % aqueous solution of $C_{19}H_{42}NBr$ (Aldrich) with equal molar exchange capacity of Amberjet 4400 (OH) ion-exchange resin (SIGMA Co.) under vigorous magnetic stirring for ~ 24 h. Silica sources were HiSil-915 from Pittsburgh Plate Glass (~ 90 wt % SiO_2 as well as 0.5 wt % $NaSO_4$), Cab-O-Sil (99.8% + SiO_2) from Cabot Corporation, and tetramethylammonium silicate (10 wt % SiO_2) from Aldrich. Typically, 2.5 g of the colloidal silica (HiSil or Cab-O-Sil) and 10.4 g of soluble silica (tetramethylammonium silicate) were dissolved in 50 mL of deionized water and stirred vigorously for 30 min. This was followed by the dropwise addition of known amounts of 2 wt % $Fe(NO_3)_3 \cdot 9H_2O$ solution corresponding to 1, 2, and 3 wt % from a pipet to the resulting mixture under vigorous stirring. After 30 min, a small amount of antifoaming agent (Antifoam A, Sigma Chemical Co.) corresponding to 0.2 wt % of surfactant was added to the mixture to improve the reproducibility and remove excess foam. The antifoaming agent is a silane polymer alkyl terminated by methoxy groups. This was followed by the addition of 28.8 g of CTMAOH and was allowed to mix for over 30 min under vigorous stirring. The pH was reduced to ~ 11 by the dropwise addition of acetic acid (Baker, 99.9%). The mixture was then transferred into a polypropylene bottle and autoclaved at 373 K for 6 days. The synthesis of Fe-free siliceous MCM-41 followed the same procedure without the addition of aqueous solution of $Fe(NO_3)_3 \cdot 9H_2O$. The final products obtained were recovered by filtration, washed with deionized water, and dried at ambient conditions for 24 h. The molar composition of the gel subjected to hydrothermal synthesis was as follows: $1.0 SiO_2:0.33 CTMAOH:xFe:yH_2O$ where $x = 0.01, 0.02$, and 0.03 ; $y = 81-104$.

The as-synthesized samples were calcined to remove the organic surfactants from the pores of MCM-41. Calcination was performed by heating from room temperature to 813 K over 20 h in a He stream ($60 cm^3/g\cdot min$) and was maintained at this temperature for 1 h in flowing He and 6 h in flowing air ($40 cm^3/g\cdot min$). All investigations have been limited to calcined samples except those involving diffuse reflectance UV–vis spectroscopy where the local environment of Fe in the as-synthesized and calcined samples have been compared.

Characterization of Catalyst. Except where stated otherwise, the catalysts synthesized from HiSil were used for all investigations.

Elemental Analysis. The final Fe content in each sample was determined by ICP measurements (Galbraith Laboratories, Inc.) because the synthesis process can result in some loss of Fe and silica in the byproduct.

X-ray Diffraction (XRD) Studies. XRD measurements were carried out using a Shimadzu X-ray diffractometer (Cu $K\alpha$, $\lambda = 0.154$ nm, 40 kV, 30 mA) to confirm the long-range order

of the characteristic hexagonal pore structure of the synthesized catalysts after calcination. The d_{100} values were obtained using the Bragg diffraction equation. The distance between the pore centers of the hexagonal structure is calculated from the relation $a_0 = 2d_{100}/\sqrt{3}$.

N_2 Physisorption. N_2 adsorption–desorption studies were carried out at 77 K with a static volumetric instrument Autosorb-1C (Quantachrome) to examine the mesoporous properties of the catalysts. Samples were pretreated by outgassing at 373 K for 30 min and at 473 K for more than 30 min to a residual pressure below 1×10^{-4} Torr. The pore size distribution (PSD) was evaluated from the desorption isotherms using the BJH method.²⁰ The results of XRD and N_2 physisorption have been used in estimating the wall thickness; it was assumed to be equal to the difference between the spacing of pore centers and the BJH pore diameter.

UV–Vis. The diffuse reflectance UV–vis spectra were recorded on a Hewlett-Packard 8452A diode array spectrometer equipped with a Harrick praying mantis. Samples were hand pressed in the sample holder to obtain a thick wafer and the spectra were collected in a range of 200–800 nm. The reference samples (Fe_2O_3 and $FePO_4$) were diluted to 1 wt % with siliceous MCM-41 before measurement.

Electron Paramagnetic Resonance (EPR). X-band EPR investigations were carried out using a Varian E-9 spectrometer (9.28 GHz/4.5 T) equipped with a TE₁₀₂ cavity and a helium flow cryostat (Oxford Instruments) at 60 K and at room temperature (298 K). Details of the experimental procedure has been described by Lakshmi et al.²¹

X-ray Absorption. Fe K -edge XANES spectra were recorded at beam line X23A2 with Si(111) as the monochromator crystal at the National Synchrotron Light Source at Brookhaven National Laboratory. The intensity of the incident beams (I_0) was determined using a 30-cm-long ion chamber filled with pure N_2 . Data were collected in transmission mode by scanning from 200 below to 1600 eV beyond the Fe K edge. Samples were pressed to self-supporting wafers and placed in a stainless steel cell for measurement. A detailed description of the procedure has been reported in ref 5.

Temperature-Programmed Reduction (TPR). The reducibility and the stability of Fe–MCM-41 samples were investigated by TPR using a TCD detector of a gas chromatograph (6890 plus, Agilent). Typically, ~ 200 mg of the catalyst was put into the quartz cell. Prior to each run, the sample cell was purged with ultra zero grade air while the temperature was increased from room temperature to 773 K at 5 K/min. After 1 h at this temperature, the catalyst was cooled to room temperature in flowing air. This pretreatment procedure produces a clean catalytic surface without altering the surface and the structure before the run is commenced. After this pretreatment, the gas flow was switched to 5% H_2 in Ar balance and the baseline was monitored until it became stable. The sample cell was then heated at 5 K/min and held for 1 h at 1173 K to ensure complete Fe reduction. An acetone trap was installed between the sample cell and the TCD to condense water produced by sample reduction.

Synthesis of CNTs. The production of CNTs by acetylene pyrolysis over Fe–MCM-41 was carried out at atmospheric pressure in a specially designed flow reactor (quartz tube of inner diameter 6.5 cm and length of 44 cm). The reactor was separated by a porous frit to enable the introduction of gas feeds through one end where the catalyst was loaded and flowed out of the reactor through the frit. A thermocouple was placed at the opposite end of the reactor, close to the catalyst bed, to

TABLE 1: Textural Properties of the Various Catalysts Synthesized from HiSil and Cab-O-Sil

colloidal silica	Fe content in synthesis gel (wt %)	Fe content in sample by ICP (wt %)	pore diameter (Å)	pore volume (cc/g)	S_{BET} (m ² /g)	d_{100} (Å)	pore wall thickness (Å)	color of calcined sample
HiSil	0		26.89	1.069	1218	35.50	14.10	white
HiSil	1.0	0.99	28.77	0.94	1073	38.50	15.68	white
HiSil	2.0	1.59	29.30	1.01	1144	39.92	16.79	pale yellow
HiSil-R ^a	2.0		25.08	0.24	304			black
HiSil-O ^b	2.0		26.23	1.167	1089			pale yellow
HiSil	3.0	2.25	28.60	0.44	514			brown
Cab-O-Sil	0		27.33	0.935	1045	38.29	16.88	white
Cab-O-Sil	1.0	0.99	29.52	0.813	898	39.61	16.24	white
Cab-O-Sil	2.0	1.78	29.38	0.87	969	41.58	18.63	pale yellow
Cab-O-Sil-R ^a	2.0		27.58	0.682	882			black
Cab-O-Sil-O ^b	2.0		26.84	0.926	990			pale yellow
Cab-O-Sil	3.0	2.37	29.37	0.80	909	42.05	19.19	brown

^a After reaction. ^b After carbon removal (TPO).

determine the exact temperature of the catalyst. The reactor was placed horizontally in a tubular electric furnace (length = 90 cm, Omega), equipped with a temperature controller. In a typical run, 0.5 g of the calcined catalyst was put into the reactor, heated in He flow (200 cm³/g-min) from room temperature to 1073 K at a heating rate of 10 K/min. Subsequently, C₂H₂/N₂ mixture (99% N₂ and 1% C₂H₂) at a flow rate of 200 cm³/g-min was fed into the reactor and maintained under these conditions for 1 h. The flow rate of the gases was controlled using Omega mass flow controllers. The reactor was then allowed to cool to room temperature in flowing He at the conclusion of each run.

Characterization of CNTs. Raman Spectroscopy. Raman spectra were obtained using a LabRam instrument from Jobin Yvon Horiba equipped with an Olympus confocal microscope using an excitation wavelength of 532 nm.

High-Resolution Transmission Electron Microscopy (HR-TEM). The TEM micrographs were recorded on a Philips Tecnai F20 TEM instrument equipped with a field emission gun and accelerating voltages of up to 200 kV. The point resolution and the line resolution were 0.24 and 0.12 nm, respectively, at a focal length of 1.7 mm. Samples were prepared by ultrasonically ~1 mg of the final product in 10 mL of ethanol (ACS/USP grade). A drop of this suspension was then put on a lacey carbon coated copper TEM grid.

3. Results and Discussion

Characterization of Catalyst. A summary of the physical properties of the catalysts used in this study is presented in Table 1. The results of ICP measurement as shown in Table 1 reveal that Fe is quantitatively incorporated at low concentration in synthesis gel, but the amount incorporated decreases as the concentration of Fe in the synthesis gel increases. Also, catalysts containing ca. 2 and 3 wt % Fe synthesized from Cab-O-Sil retained more Fe than those from HiSil. The high purity of Cab-O-Sil (>99.8%) may be responsible for this observation because HiSil contains impurities, which may compete for different sites with incorporated Fe in the silica.

In this study, comparisons of the mesoporous structural integrity and stability of the catalytic templates containing ca. 1, 2, and 3 wt % Fe synthesized from HiSil and Cab-O-Sil have been carried out. On the basis of the ICP results presented in Table 1, catalysts containing ca. 2 wt % Fe synthesized from HiSil and Cab-O-Sil are actually a 1.59 wt % Fe (HiSil) to a 1.78 wt % Fe (Cab-O-Sil) and the 3 wt % is actually a 2.25 wt % Fe (HiSil) to a 2.37 wt % Fe (Cab-O-Sil).

XRD pattern of siliceous MCM-41 and Fe-containing MCM-41 (Fe = 1, 2, 3 wt %) synthesized using HiSil and Cab-O-Sil

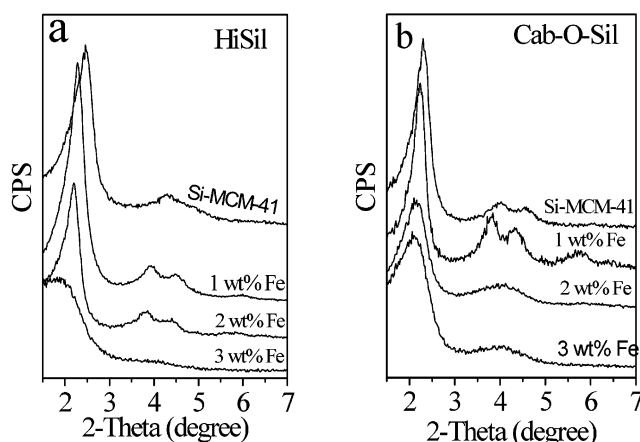


Figure 1. XRD patterns of calcined siliceous MCM-41 and Fe–MCM-41 containing different Fe loadings synthesized using HiSil (a) and Cab-O-Sil (b).

silica are shown in Figure 1a and 1b, respectively. The XRD patterns of all HiSil and Cab-O-Sil samples are consistent with that reported for MCM-41 by Beck et al.¹ They are characterized by a strong, narrow, low-angle reflection at about $2\theta = 2^\circ$ ascribed to the (100) reflection and a series of weak peaks in the range of $2\theta = 3\text{--}8^\circ$ as shown in Figure 1. These reflections arise from the ordered hexagonal array of parallel mesopores. Higher reflections corresponding to (110), (200), and (210) were well resolved for Fe–MCM-41 (1 wt %) illustrating the high regularity of the structure of this catalyst in comparison to the other catalysts. Upon Fe incorporation, the main diffraction peak {(100) reflection} is shifted to lower 2θ values indicating an increase in the lattice parameters (d -spacing and a_0 values). The corresponding lattice parameters of all the catalysts are summarized in Table 1. Given that all template synthesis parameters were kept constant, the increase in the lattice parameter could be considered as a proof of the isomorphous substitution of Si⁴⁺ ions with those of Fe³⁺ in the framework. This is because the ionic radii of Fe³⁺ (0.65 Å) are much larger than Si⁴⁺ (0.26 Å). Consequently, the Fe–O bond length is greater than that of Si–O. The absence of a well-defined (100) reflection for Fe–MCM-41 (3 wt %), especially for samples synthesized from HiSil, shows that there is a significant decrease in the structural regularity of the sample upon the introduction of ca. 3 wt % Fe. No peaks were observed in the high-angle range of all samples suggesting the absence of any crystalline phases. This, however, does not rule out the existence of iron species at the surface because of the limitation of XRD to detect very small particles at low concentrations. The brown color of Fe–MCM-

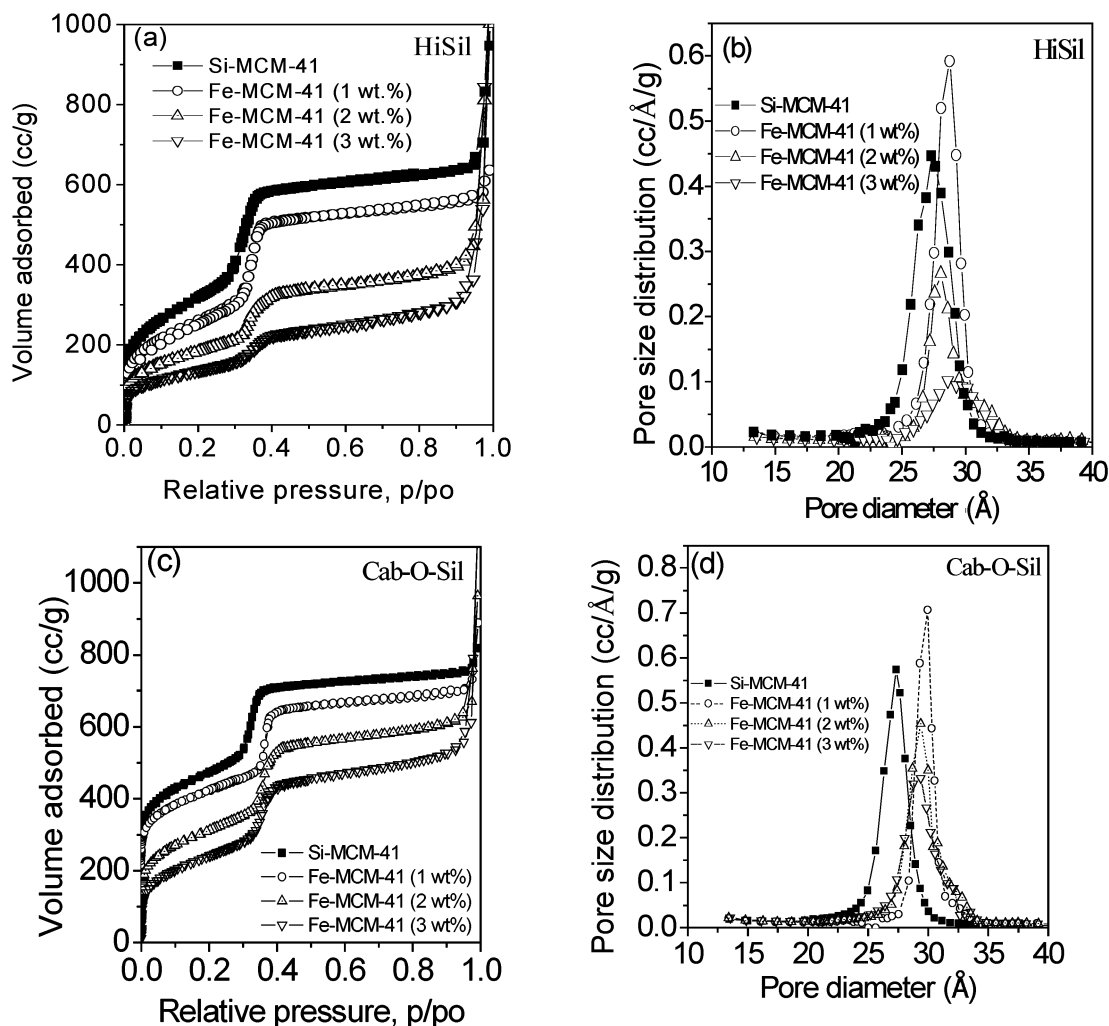


Figure 2. N₂ adsorption–desorption isotherms of Si–MCM-41 and Fe–MCM-41 (1, 2, and 3 wt %) and their respective pore size distributions synthesized from HiSil (a) and (b) and Cab-O-Sil (c) and (d).

41 (3 wt %), however, is suggestive of the presence of iron oxides.^{22,23}

The results of both XRD and N₂ physisorption are complementary with respect to probing the structural integrity of MCM-41. XRD can be used to characterize the two-dimensional hexagonal structure of the catalyst while N₂ physisorption gives information about the extent of the uniformity of the mesopores. While XRD characterizes only the ordered portion of the material, N₂ physisorption gives a volume average measure of order and thus gives a complementary picture of the overall structure of the material. The N₂ adsorption–desorption isotherm and PSD of siliceous MCM-41 and Fe–MCM-41 (1, 2, and 3 wt %) synthesized from HiSil are presented in Figure 2a and 2b, while those synthesized from Cab-O-Sil are shown in Figure 2c and 2d. The isotherms of all samples show a sharp inflection step at p/p_0 of ~ 0.3 – 0.4 , characteristic of capillary condensation of uniform mesoporous materials.²⁴ As shown in Table 1, all samples (except Fe–MCM-41, 3 wt %) exhibited relatively high surface areas and pore volumes. The mesopore diameter observed for all samples containing Fe was about 29 Å and was unaffected by the introduction of more Fe³⁺ cations. Siliceous MCM-41 showed pore diameters (~ 27 Å) somewhat lower than those of Fe–MCM-41. The pore volume does not seem to be affected significantly by the incorporation of Fe. Generally, the pore wall thickness of MCM-41 increases with the Fe loading (Table 1) and this may be due to the longer Fe–O bond length in comparison to that of Si–O. Samples synthesized

from HiSil showed greater increase in wall thickness upon the incorporation of higher Fe loadings.

The isotherm corresponding to $p/p_0 < 0.3$ represents the monolayer adsorption of N₂ on the walls of the mesopore, while that with $p/p_0 > 0.4$ represents the multilayer adsorption on the outer surface of the particles. The point at which the inflection begins is related to the capillary condensation within the uniform mesopores and their diameter. There was a slight shift in the inflection step toward higher p/p_0 upon the introduction of Fe. This signifies an increase in pore size, in consonance with XRD results. There was no noticeable shift in the inflection step of Fe–MCM-41 upon incorporation of more Fe³⁺ cations. A hysteresis loop was observed for Fe–MCM-41 (3 wt %) at $p/p_0 > 0.9$, which is likely due to the interparticle spaces.

As shown in previous studies,^{4,25} the slope or the steepness of the capillary condensation step and the full width at half-maximum (fwhm) of the PSD curve can be used as structural indexes to assess the mesoporous structural integrity and stability of these catalysts. As shown in Figure 3a, the value of the slope increased upon the initial introduction of Fe (1 wt %) into the silica framework because of the knitting effect in consonance with previous observation.⁴ Further increase in the amount of Fe (> 1 wt %) resulted in a decrease in the value of slope, which could be attributed to the oversaturation of Fe³⁺ in the pore walls of MCM-41. The effect of Fe loading on the fwhm of the PSD curve is shown in Figure 3b. There is a general decrease in the fwhm of the PSD curve upon the incorporation of 1 wt

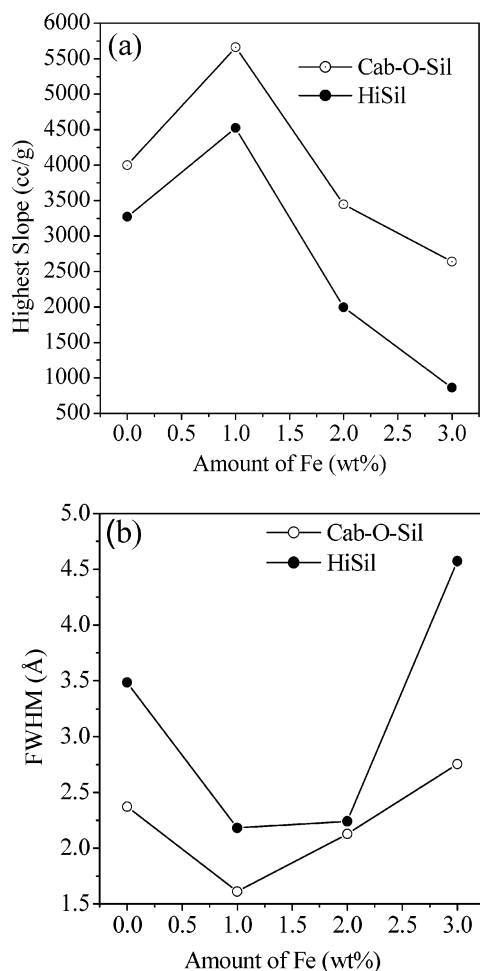


Figure 3. Effect of Fe amount on the slope of the capillary condensation step (a) and the fwhm (b) derived from Figure 2.

% of Fe. However, as the Fe amount in MCM-41 is increased beyond 1 wt %, the fwhm increases suggesting a decrease in the structural order. The behaviors of the fwhm of the PSD curves and of the slopes of the capillary condensation steps upon incorporation of different concentrations of Fe into MCM-41 are in consonance. We therefore conclude as follows: (i) there is a significant structural improvement upon the incorporation of 1 wt % of Fe into MCM-41, but a decrease in the structural integrity is observed upon incorporation of higher Fe concentrations, (ii) siliceous MCM-41 and Fe-MCM-41 synthesized from Cab-O-Sil have higher structural order in comparison to those synthesized from HiSil, as evidenced by their higher values for capillary condensation slopes and lower fwhm of the PSD curves. The specific reason for this behavior is not well understood, but it is assumed that the type and the amount of impurities present in these colloidal silica and their synthesis routes may rationalize this observation.

The UV-vis diffuse reflectance spectra in the wavelength range of 200–800 nm of Fe-MCM-41 (1, 2, and 3 wt % Fe) and reference materials of Fe^{3+} in different environments (FePO_4 and Fe_2O_3) are shown in Figure 4. Fe^{3+} in FePO_4 and Fe_2O_3 exist in tetrahedral and octahedral coordination, respectively.^{26,27} As shown in Figure 4a, isolated tetrahedral coordination of Fe^{3+} ions are characterized by a significant absorption in the wavelength range of 200–330 nm with a distinct peak at ~260 nm. On the other hand, Fe species having octahedral coordination exhibit a broad absorption band around 320–640 nm with an absorption maximum ~500 nm.

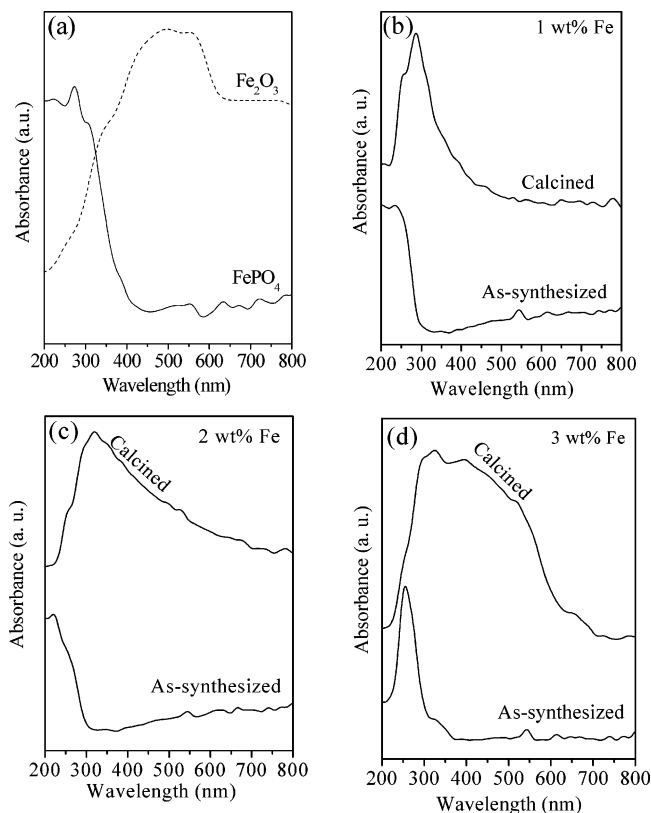


Figure 4. DR UV-vis spectra of reference compounds (a) and as-synthesized and calcined Fe-MCM-41 containing 1 wt % Fe (b), 2 wt % Fe (c), and 3 wt % Fe (d).

The absorption at 260 nm represents the oxygen ligand to metal charge-transfer transitions associated with Fe^{3+} species in isolated tetrahedrally coordinated sites.^{22,23,26–29} All the as-synthesized samples were white and showed significant absorption at 260 nm suggesting the dominance of framework incorporated Fe in the samples. Upon calcination, Fe-MCM-41 (1 wt %) retains its white color while Fe-MCM-41 (2 wt %) and Fe-MCM-41 (3 wt %) became pale yellow and brown, respectively (Table 1). As observed in Figure 4b, calcined Fe-MCM-41 (1 wt % Fe) shows an absorption peak having a maximum at 300 nm and a shoulder at 260 nm, characteristic of framework or tetrahedrally coordinated Fe. For this catalyst, most Fe seems to remain incorporated into the silica framework forming Fe–O–Si bonds. The absence of significant absorption beyond 320 nm is indicative of the absence of substantial amount of extraframework Fe confirming that most of the Fe is incorporated in the pore wall. In contrast, broadening of the absorption band to higher wavelength for calcined Fe-MCM-41 containing ca. 2 and 3 wt % Fe is observed (Figure 4c and 4d). This is suggestive of the presence of Fe^{3+} species in octahedral environment in these catalysts or of the formation of iron oxide clusters because, as shown in Figure 4a, contribution from iron oxide could also result in the broadening of the UV-vis spectra of Fe-MCM-41. The existence of extraframework, or bulk iron oxide, is usually indicated by an off-white or brown color in zeolitic²² or MCM-41²³ catalysts. The respective pale yellow and brown colors observed in Fe-MCM-41 (2 wt %) and Fe-MCM-41 (3 wt %) upon calcinations could be due to the migration of Fe species from the framework. These Fe species may exist as aggregated oxidic nanoclusters in extraframework environment. Generally, there is a shift of the absorption band to longer wavelength with increasing Fe loading. Even though calcination provokes the migration of Fe

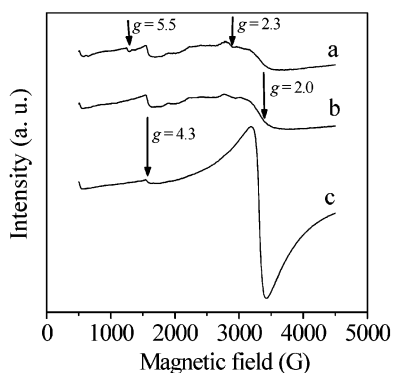


Figure 5. EPR spectra of Fe-MCM-41 containing 1 wt % Fe (a), 2 wt % Fe (b), and 3 wt % Fe (c) recorded at room temperature (298 K).

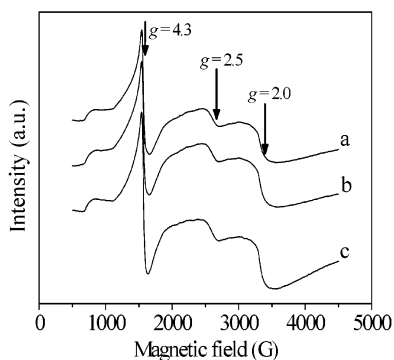


Figure 6. EPR spectra of Fe-MCM-41 containing 1 wt % Fe (a), 2 wt % Fe (b), and 3 wt % Fe (c) recorded at 60 K.

species from the framework of calcined Fe-MCM-41 (2 and 3 wt % Fe), the UV-vis spectra (Figure 4) gives evidence for the presence of framework Fe in these catalysts as evidenced by an absorption shoulder ~ 260 nm. The migration of Fe from the framework of Fe-silicate upon the alkyl template removal during calcination in air has been reported.^{27,30}

Further characterization of the local environment of Fe has been carried out by EPR spectroscopy at room temperature (298 K) and at 60 K as presented in Figures 5 and 6, respectively. EPR is a highly sensitive tool for probing the local symmetry of Fe because of its paramagnetic nature in the low-spin and high-spin electronic configurations.³¹ The interpretation of EPR data of Fe states in zeolites or MCM-41 is still an issue of controversy because the presence of surrounding silanol groups and H₂O molecules tends to interfere with the signal.³¹ The unambiguous interpretation of EPR data of Fe-MCM-41 can be accomplished if combined with results of other spectroscopic techniques such as UV-vis, Mössbauer, or X-ray absorption. On the basis of most studies carried out on Fe-containing zeolites,³¹ HMS²⁹ and MCM-41,^{23,28,32} the signal corresponding to $g = 4.3$ is considered as evidence of framework Fe and is characteristic of isolated Fe³⁺ paramagnetic cations in a strong rhombic distorted tetrahedral coordination; the signal at $g = 2$ has been assigned to extraframework Fe³⁺ or Fe³⁺ species in octahedral coordination. As observed by Goldfarb et al.,³¹ this signal at $g = 2$ could also be partly due to Fe³⁺ in tetrahedral site even though Fe³⁺ in oxidic clusters is known to give a signal at $g = 2$. The signal at $g = 2.3$ – 2.5 is ascribed to iron clusters or iron oxide species.²⁹

The EPR spectra of Fe-MCM-41 containing different loadings of Fe recorded at room temperature (Figure 5) exhibits a weak signal at $g = 4.3$ ascribed to Fe³⁺ in distorted tetrahedral coordination and a broad signal at $g = 2.0$ indicating the presence of either framework or extraframework Fe³⁺. A weak

signal is also observed at $g = 5.5$ for catalysts containing 1 wt % Fe. This signal is assigned to Fe³⁺ in less distorted tetrahedral sites. The fact that only Fe-MCM-41 (1 wt %) shows this signal confirms the incorporation Fe³⁺ species in very stable sites in this sample. The intensity of the $g = 4.3$ signal decreases with increasing Fe loading suggesting that the amount of Fe³⁺ in tetrahedral sites decreases with increasing Fe loading. Also, there is a conspicuous increase in the line intensity of the $g = 2$ signal with increasing Fe loading which indicates an increase in the Fe amount in octahedral coordination. These results are consistent with those of UV-vis spectroscopy.

Conversely, the spectra of Fe-MCM-41 recorded at 60 K showed a strong signal at $g = 4.3$ and a broad signal at $g = 2.0$ (Figure 6). The line intensity of the $g = 4.3$ signal increases slightly with Fe amount while a more pronounced increase was observed for the $g = 2.0$ signal. The behavior of the $g = 2.0$ signal is similar to that recorded at room temperature. The signal observed at $g = 4.3$ or higher g values is temperature dependent and the intensity generally decreases with increasing temperature and tends to disappear at room temperature because of the faster spin relaxation.³¹ In a qualitative sense, the presence of an intense $g = 4.3$ signals for all samples is an indication that all these catalysts have Fe³⁺ in distorted tetrahedral sites.

In consonance with results of UV-vis, it can be concluded that despite the dislodgement of Fe species from the framework as a result of calcination, framework Fe species still exist in a relatively high amount in both Fe-MCM-41 (2 wt %) and Fe-MCM-41 (3 wt %). The signal attributed to the iron oxide species occurs at a g value range of 2.2–2.5. For spectra recorded at room temperature, this signal is observed at $g = 2.3$ but at lower temperature (60 K) it is observed at $g = 2.5$. The presence of a well-defined signal at $g = 2.5$ signifies the presence of iron oxide species in all the catalysts regardless of the Fe loading. The line intensities of this signal for catalysts containing ca. 1, 2, and 3 wt % Fe were 40, 42, and 49, respectively. This suggests that there is a saturation of Fe cations in the pore walls and the surpluses form extraframework species at the surface. This confirms the increase in the amount of iron oxide with Fe loading as qualitatively indicated by the colors of the samples.

The coordination geometry of Fe in these catalysts was also characterized by X-ray absorption spectroscopy. The preedge feature of Fe in X-ray absorption near-edge structure (XANES) spectra is very sensitive to the local coordination status. The position, intensity, and shape of the preedge peaks observed are related to the local environment of Fe species and its electronic structure. The normalized near-edge region of XANES spectra of Fe-MCM-41 containing various Fe loading and Fe₂O₃ is shown in Figure 7a. The enlarged preedge region of the catalysts is shown in Figure 7b. Fe³⁺ in tetrahedral coordination is characterized by a single well-defined preedge peak, attributed to the $1s \rightarrow 3d$ dipolar transition (Figure 7a).^{26,27} This transition is forbidden for octahedral coordination, but is usually present, albeit of low intensity, for distorted octahedral coordination as confirmed by the relative low intensity of the preedge peak of Fe₂O₃. The intensity of the preedge feature is related to the coordination number of the transitional metal. As the intensity decreases, there is a change in the coordination environment of the metal from tetrahedral \rightarrow distorted tetrahedral \rightarrow pyramidal \rightarrow distorted octahedral \rightarrow octahedral. On the basis of the preedge features and their corresponding intensities observed for these catalysts, it is obvious that Fe³⁺ in Fe-MCM-41 (1 wt %) exists mainly in tetrahedral environment, evidenced by the high intensity. The intensity decreases

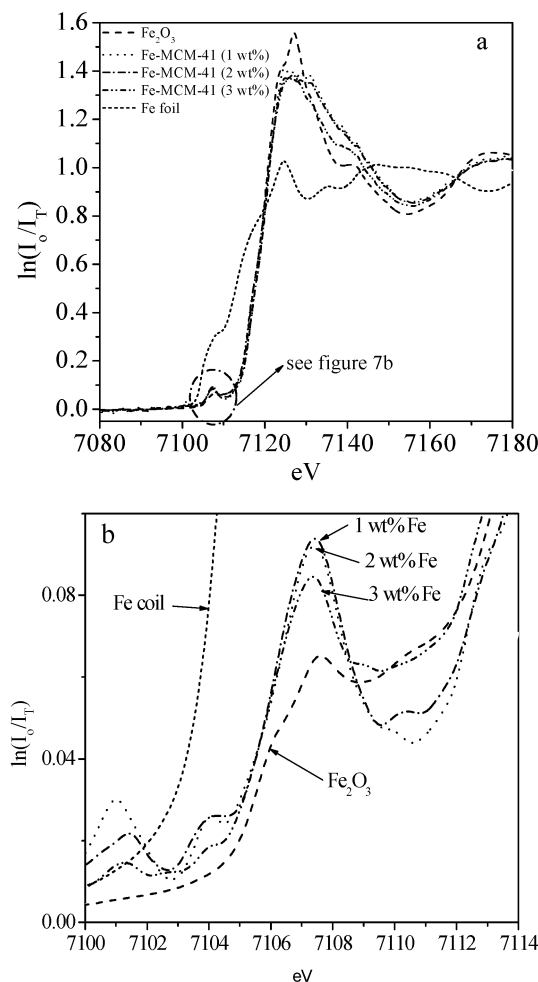


Figure 7. Fe *K*-edge XANES spectra for Fe-MCM-41 containing different Fe loading (a) and their enlarged pre-edge features (b).

slightly for catalysts containing 2 wt % Fe suggesting the gradual change from tetrahedral to distorted coordination by some Fe species. However, catalysts containing 3 wt % Fe showed a pre-edge peak of low intensity suggesting the dominance of distorted and octahedrally coordinated Fe species resulting from surface Fe oxide species. The decrease in the pre-edge peak intensities with increasing the Fe loading observed in these catalysts may be rationalized by Laporte law. As explained by this law, the $A_{1g} \rightarrow T_{2g}$ and $A_{1g} \rightarrow E_g$ transitions are symmetrically forbidden in the octahedrally coordinated Fe^{3+} species, even though they are allowed for distorted octahedral symmetry, while the $A_1 \rightarrow T_2$ transition is allowed for Fe^{3+} species in tetrahedral sites. It is evident from these results that the fraction of Fe^{3+} species in tetrahedral coordination decreases with increasing Fe loading. This conclusion is consistent with the results of EPR and UV-vis.

TPR has been employed to investigate the reduction characteristics of Fe. The TPR profiles of Fe-MCM-41 containing different loadings of Fe are shown in Figure 8. The main feature of the TPR profiles of Fe-MCM-41 (1 wt %) and Fe-MCM-41 (2 wt %) is a distinct reduction peak with maximum at 675 and 653 K, respectively, while that of Fe-MCM-41 (3 wt %) shows three defined peaks in the temperature range of 600–850 K. The Fe-MCM-41 (3 wt %) has a reduction rate similar to Fe-MCM-41 (2 wt %) evidenced by their similar reduction peak maxima at 653 K. This suggests a similarity in the local environment of the Fe^{3+} species present in these catalysts. The reduction temperature of Fe-MCM-41 (1 wt %) is slightly

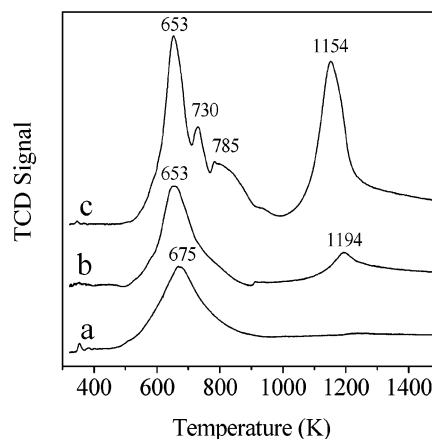


Figure 8. TPR profiles of Fe-MCM-41 containing 1 wt % Fe (a), 2 wt % Fe (b), and 3 wt % Fe (c).

higher than Fe-MCM-41 containing ca. 2 and 3 wt % Fe. This is not surprising because more framework Fe species exist in stable tetrahedral sites in Fe-MCM-41 (1 wt %) than in the other samples, as confirmed by spectroscopic data. As observed in the TPR profile of Fe/SiO₂ with high Fe loading (2.9 wt %),³³ the three reduction peaks we observed in the profile of Fe-MCM-41 (3 wt %) can also be accounted for by the three steps of iron oxide reduction: $Fe_2O_3 \rightarrow Fe_3O_4 \rightarrow FeO \rightarrow Fe$. A second peak is also observed at higher reduction temperature (>1000 K), and its intensity increased with the Fe loading. This peak is not visible in Fe-MCM-41 (1 wt %) because of the scale used. As shown by the TPR profiles of reference compounds (Fe_2O_3 and Fe_3O_4),³⁴ the complete reduction of Fe^{3+} and Fe^{2+} is generally completed at temperatures lower than ~973 K. This suggests that the second peak observed in the TPR profiles of our catalysts is not associated with any of the reduction steps of Fe. High-temperature peaks of this nature have been observed in the TPR profiles of Co-MCM-41 performed in our laboratory and have been attributed to the reduction of cobalt silicate formed during high-temperature treatment.³⁵ It is therefore assumed here that the reduction of Fe-silicate produced during the course of increasing the temperature accounts for the high-temperature reduction peak observed in these profiles.

Characterization of CNTs. The products obtained from the pyrolytic decomposition of acetylene over these catalysts have been characterized by Raman spectroscopy, thermogravimetry, and TEM. A typical Raman spectrum of CNTs is characterized by a D-band, G-band, and in some cases a radial breathing mode (RBM). The D-band is associated with the amount of disordered carbon and occurs in the 1200–1400 cm^{-1} part of the spectrum. The G-band reveals the intense tangential modes of CNTs and the good arrangement of the hexagonal lattice of graphite, which occurs in the high-frequency region of 1500–1600 cm^{-1} . The RBM usually occurring in the low-frequency region (100–250 cm^{-1}) is generally considered as a special signature of SWNT. The frequencies of the RBM are inversely proportional to the nanotube diameters. The carbon loading in the product was determined gravimetrically by air oxidation under a programmed temperature between 373 and 1173 K at 10 K/min.

Because of the high reactivity of acetylene, previous investigators³⁶ have shown that a narrower range of operating conditions exists for selective production of SWNT when compared to the CO disproportionation process. Preliminary studies using Fe-MCM-41 (2 wt % Fe) were carried out to determine the optimal temperatures, reaction times, and reactant flow rates. In general, we find that for a 60-min growth run using a reactant flow rate of 200 mL/g-min at 973 K, few

TABLE 2: Summary of the Carbon Yields and the Carbon Species Obtained from the Reaction Catalyzed by the Various Catalysts Synthesized from Different Colloidal Silica HiSil and [Cab-O-Sil]

catalyst	Fe content in synthesis gel (wt %)	carbon yields ^b (wt %)	carbon species ^a
Si-MCM-41	0	8.49 [7.23] ^c	amorphous carbon
Fe-MCM-41	1.0	9.70 [9.17]	amorphous carbon graphite
Fe-MCM-41	2.0	10.55 [9.84]	SWNT MWNT graphite amorphous carbon
Fe-MCM-41	3.0	5.36 [7.23]	MWNT graphite amorphous carbon

^a On the basis of HR-TEM studies. ^b Determined by gravimetric analysis. ^c Values in brackets are for samples synthesized from Cab-O-Sil.

SWNTs are produced. However, the yield of SWNTs increased for samples synthesized at 1073 K and as the temperature is increased further, MWNT becomes predominant.

Studies of the effect of Fe amount on the production of CNTs were carried out at 1073 K using a C₂H₂/N₂ flow rate of 200 cm³/g-min for 60 min, the optimal experimental conditions for high selectivity of CNTs during acetylene decomposition over Fe-MCM-41. Total carbon yields measured by thermogravimetry is expressed in terms of weight percent (wt %) and are given in Table 2. An increase in carbon yield was observed for catalysts containing 1 and 2 wt % of Fe. Catalysts containing 3 wt % of Fe showed slightly lower activity for carbon production as evidenced by their lower carbon yields of ~5–7 wt %. Indiscriminate production of carbon was observed even in the absence of a metal catalyst evidenced by the high carbon yield (~8 wt %) obtained for reactions carried out over Fe-free siliceous MCM-41. This may be attributed to the self-pyrolysis of acetylene at high temperature to form high deposits of undesired carbonaceous material, such as amorphous carbon. Siliceous MCM-41 synthesized from HiSil showed slightly higher activity toward carbon production than those from Cab-O-Sil. This behavior was also observed for Fe-MCM-41 samples except those containing 3 wt % Fe. The presence of some metal impurities in HiSil could be responsible for the higher reactivity associated with catalysts synthesized from HiSil.

Despite the high carbon yields observed in the products of reactions catalyzed by siliceous MCM-41, Raman studies revealed the absence of CNTs as evidenced by their featureless spectra (not shown). The Raman spectra of products obtained from reactions catalyzed by Fe-MCM-41 (1 wt %) also showed a similar result (not shown). The absence of any of the characteristic bands of CNTs in these products suggests that reactions involving these catalysts result in the formation of undesired carbonaceous species. This conclusion was also reached after the samples were studied by HR-TEM. The Raman spectra of products obtained from reactions over Fe-MCM-41 (2 wt %) and Fe-MCM-41 (3 wt %) are shown in Figure 9. Product formed over Fe-MCM-41 (2 wt %) shows a distinct G-band, which is accompanied by the presence of an RBM (insert of Figure 9), while that formed over Fe-MCM-41 (3 wt %) shows a G-band of comparatively low intensity and no RBM. There are several RBM peaks in the range of 175–333 cm⁻¹, which corresponds to SWNT diameters in the range of 0.67–1.28 nm on the basis of the following relationship, $\omega_r =$

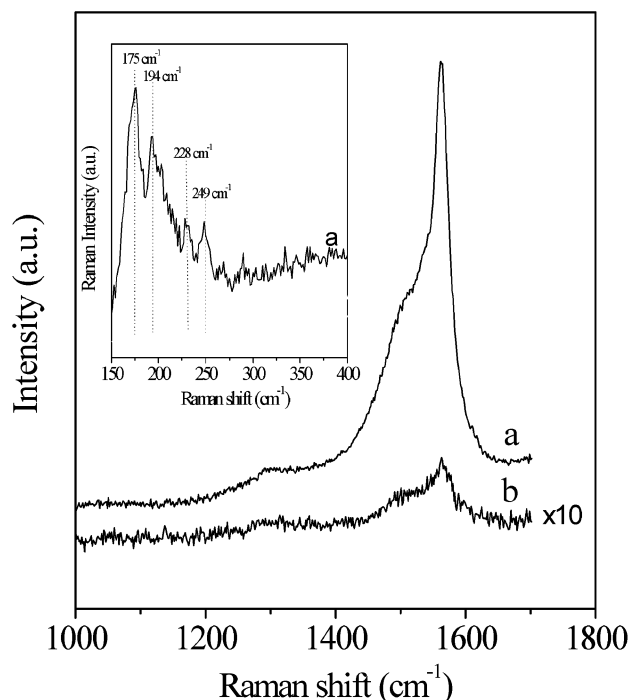


Figure 9. Raman spectra of CNTs synthesized over Fe-MCM-41 containing 2 wt % Fe (a) and 3 wt % Fe (b) at 800 °C for 1 h using reactant flow rate of 200 sccm.

$223.75 \text{ (cm}^{-1} \text{ nm)}/d \text{ (nm)}$,³⁹ where ω_r and d are the RBM frequency and the tube diameter, respectively. It is expected that if other tube diameters are present they cannot be detected with a single wavelength experiment (532 nm) because of their diameter-dependent resonances. Thus, the range of the diameter distribution of these CNTs cannot be determined. The relatively low intensity of the D-band observed in both spectra illustrates the absence of large amounts of amorphous carbon if reactions are carried out at these optimized conditions. It is evident from this result that under these reaction conditions, Fe-MCM-41 (2 wt %) shows selectivity for SWNT production while Fe-MCM-41 (3 wt %) are selective for MWNT production. Even though the source of colloidal silica affected the activity of Fe-MCM-41, no noticeable difference in their selectivity for CNT production was observed. The Fe loading and the local environment of Fe in MCM-41 were observed to be key factors in determining selectivity toward CNTs.

Figure 10 shows representative HR-TEM images of the products of the reaction over siliceous MCM-41 and Fe-MCM-41 containing various Fe loadings. Amorphous carbon was the main carbon material observed in the products of reactions catalyzed by Si-MCM-41 and Fe-MCM-41 (1 wt %) as shown in their TEM micrographs (Figure 10a and 10b). However, some graphitic materials were observed in the products obtained from reactions catalyzed by Fe-MCM-41 (1 wt %). We observed mostly bundles of SWNT (Figure 10c and 10d) along with fewer individual SWNTs in the products obtained from reactions catalyzed by Fe-MCM-41 (2 wt %). Also, some MWNTs covered with amorphous carbon were observed. The TEM image of product of reaction catalyzed by Fe-MCM-41 (3 wt %) shows the presence of large Fe metal particles with a graphitic layer covering (Figure 10e). Although not shown here, MWNTs were also observed for this catalyst. The actual amount of CNTs present in these products has not been determined because of the difficulty associated with the quantification of CNTs. However, on the basis of TEM studies, qualitative thermogravimetric analysis, and Raman spectroscopy (low D/G band ratio),

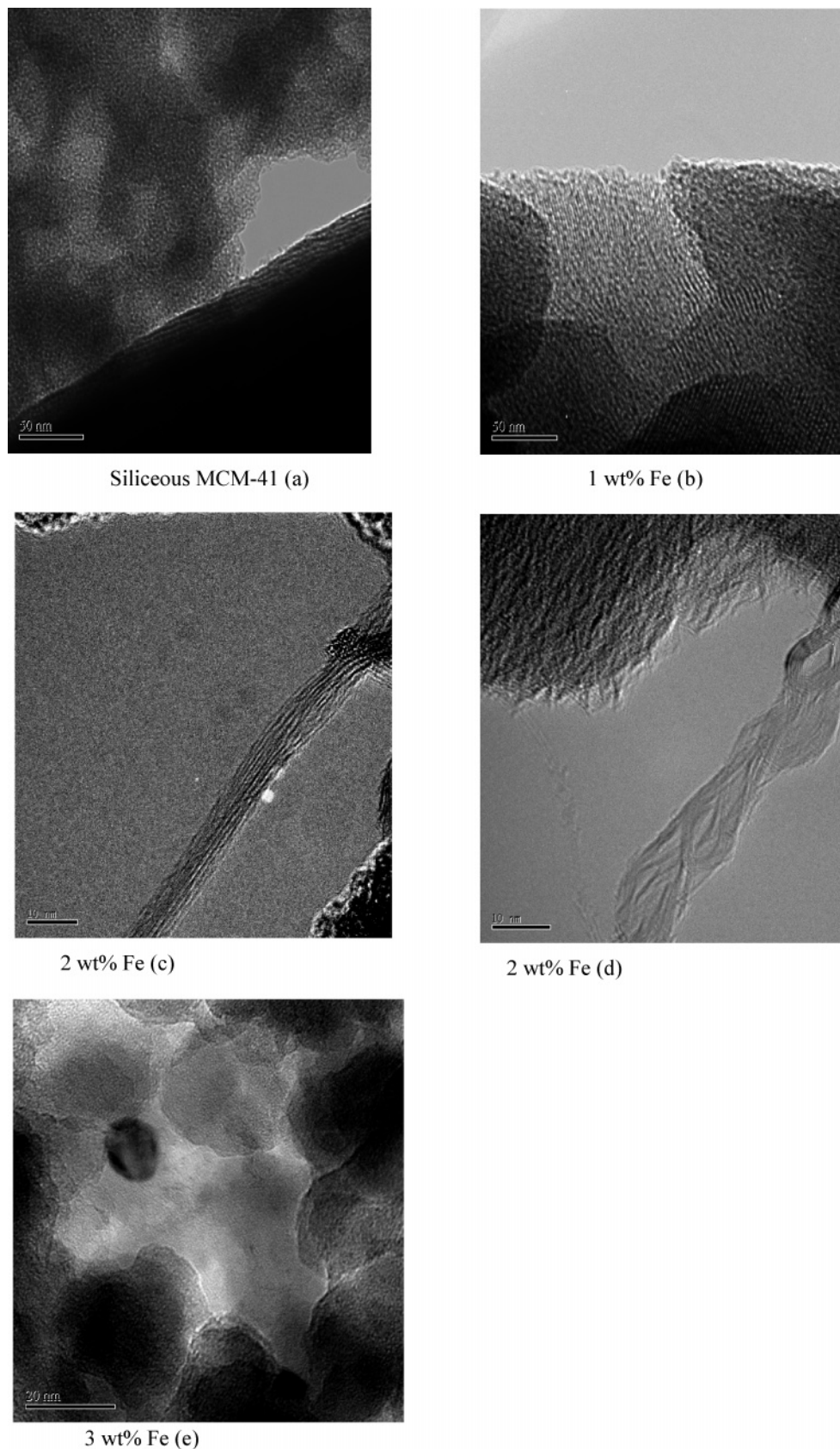


Figure 10. HR-TEM micrographs of carbon products formed over the various catalysts as labeled.

large amounts of CNTs of relatively high quality and purity were produced.

Local Environment of Fe after Reaction. The catalytic templates (Fe-incorporated MCM-41 with different loadings) were characterized by EPR at 60 K to probe the local

environment and state of Fe after the reaction. Figure 11 shows the EPR spectra of the different catalysts before and after the reaction. As mentioned previously, the EPR signal corresponding to $g = 4.3$ is ascribed to high-spin Fe^{3+} species in distorted tetrahedral coordination. For all the fresh catalysts, the intensities

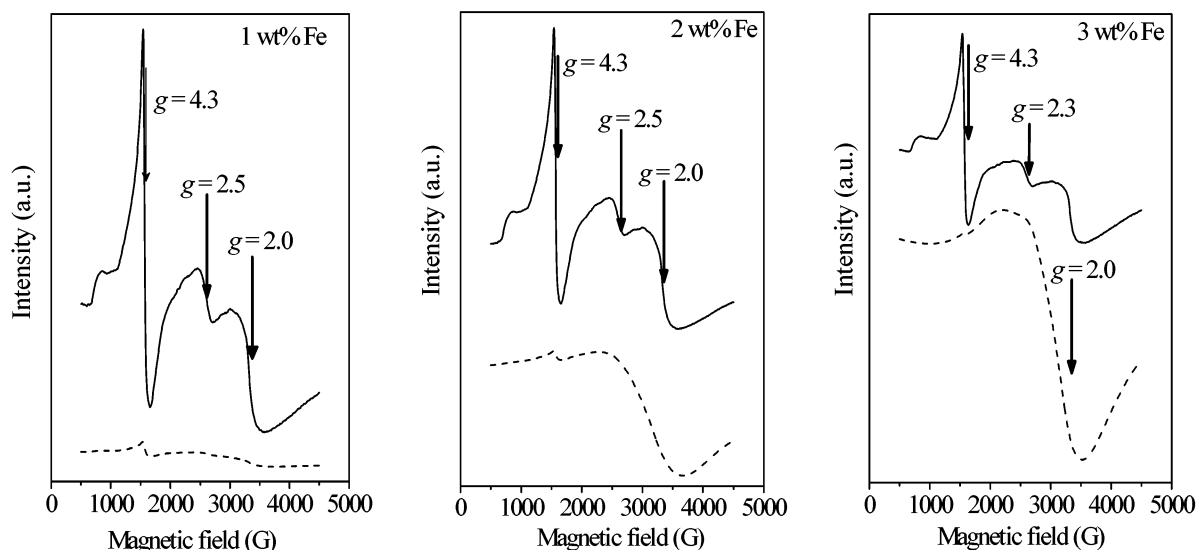


Figure 11. EPR spectra of Fe-MCM-41 containing 1 wt % Fe (a), 2 wt % Fe (b), and 3 wt % Fe (c) recorded at 60 K before (bold lines) and after (dashed lines) reaction.

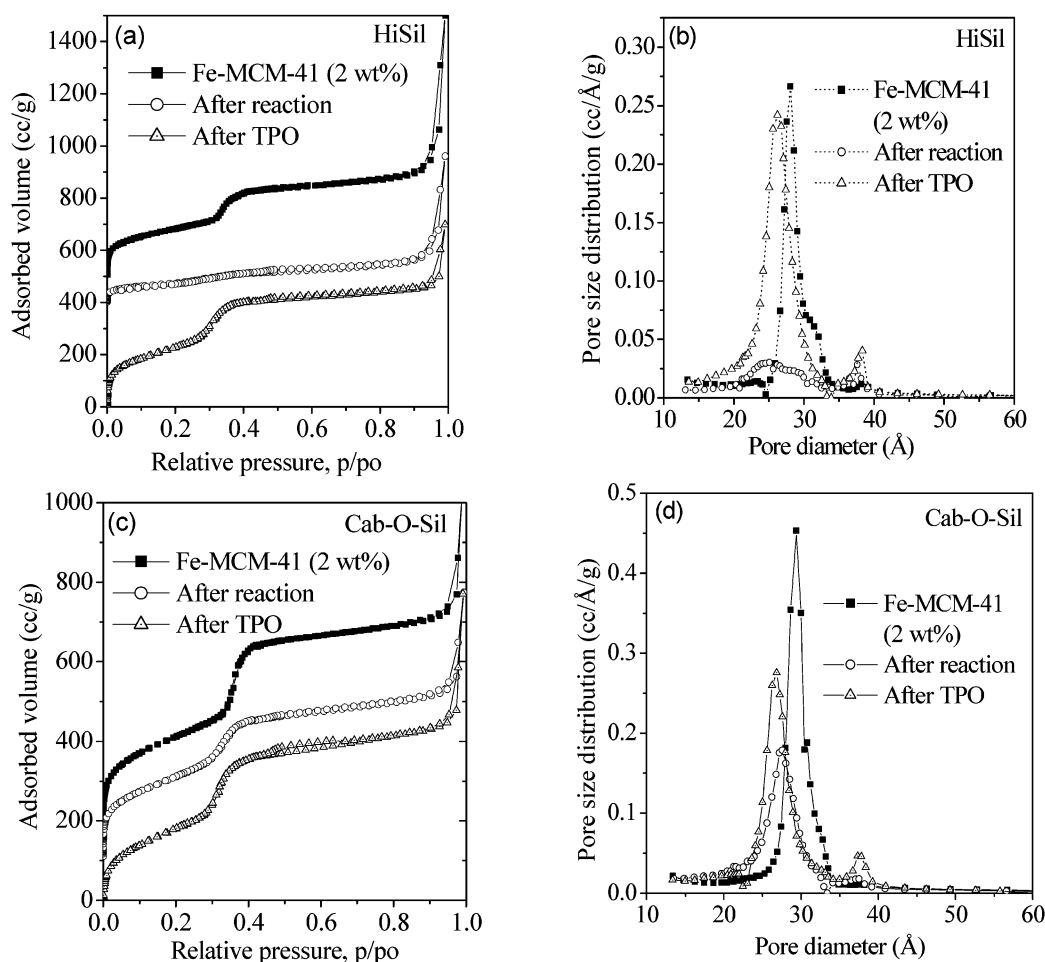


Figure 12. N_2 adsorption-desorption isotherms and their respective pore size distributions of Fe-MCM-41 (2 wt %) after reaction and carbon removal (TPO) synthesized from HiSil (a) and (b) and Cab-O-Sil (c) and (d).

of the $g = 4.3$ signals are higher than their corresponding $g = 2.0$ signal. This is, however, not the case for the used catalyst particularly for catalysts containing ca. 2 and 3 wt % Fe as the intensities of their $g = 2.0$ signals become dramatically higher than their $g = 4.3$ signal. It was also observed that the $g = 4.3$ signal diminished for catalysts containing ca. 1 and 2 wt % Fe after the reaction, and for catalysts containing 3 wt % Fe this

signal disappears completely. This reveals that the Fe^{3+} species still exist in tetrahedral environment for catalysts containing ca. 1 and 2 wt % Fe even after the reaction. The migration of Fe^{3+} species of Fe-MCM-41 from its framework positions to extraframework environment increases in the following order of Fe amount in synthesis gel: 1 wt % Fe < 2 wt % Fe < 3 wt % Fe. In situ reduction of Fe by the hydrogen produced during

acetylene decomposition is believed to occur, and this process is responsible for the formation of metallic Fe, which likely provides the “seeds” for SWNT nucleation. As observed in a recent study,³⁷ the size of the metallic clusters formed is determined by the radius of curvature of the pore size of MCM-41. The mechanism associated with the formation of these metal clusters in MCM-41 has been addressed in another study.³⁸ Reduction may induce the migration of Fe species from framework to extraframework environment. In general as observed in Fe-silicates, upon reduction the $g = 4.3$ signal should decrease in intensity while its corresponding $g = 2.0$ signal should increase. However, it is of interest that in situ reduction had very little effect on Fe–MCM-41 (1 wt %) as shown in their EPR spectra (Figure 11a) probably because of the higher stability of Fe in the framework. The signal at $g = 2.5$ for all samples disappears after the reaction and indicates the reduction of these surface iron oxide species to metallic Fe.

Stability of Fe–MCM-41. For Fe–MCM-41 to be used as good catalytic templates for CNTs synthesis, it is important that it shows good stability under the reaction conditions which include carbon deposition at high temperature and oxidation. The structural stability of Fe–MCM-41 (2 wt %) after reaction and temperature-programmed oxidation (TPO) was assessed by N₂ physisorption, Figure 12. Catalysts synthesized from Cab-O-Sil were more stable and maintained their high mesoporous structural integrity after the reaction better than those synthesized from HiSil. The N₂ adsorption–desorption isotherm of the former still showed a distinct capillary condensation step at p/p_0 of ~ 3.5 (highest slope = 1330) while the latter showed an inconspicuous step (highest slope = 239). After the reaction, Fe–MCM-41 (Cab-O-Sil) still maintained a fairly narrow PSD as the fwhm increased from 1.72 Å for fresh catalyst to 3.84 Å while that of Fe–MCM-41 (HiSil) shows a broad PSD, evidenced by the dramatic increase in the fwhm from 2.29 Å to 9.31 Å. This suggests that the uniform mesoporous structure of the HiSil catalyst is either destroyed or the pores are largely blocked after carbon deposition. As shown in Table 2, the carbon yields obtained for reactions catalyzed by Fe–MCM-41 (Cab-O-Sil) and Fe–MCM-41 (HiSil) containing 2 wt % Fe were 9.84 and 10.55 wt %, respectively. The difference in carbon yields of these samples is quite insignificant and does not seem to account for the loss of porosity of Fe–MCM-41 synthesized from HiSil. As expected, there was a general decrease in the pore diameter, pore volume, and S_{BET} upon carbon deposition as shown in Table 1. This decrease was much higher for Fe–MCM-41 (HiSil) samples. After carbon removal via TPO in air between 373 and 1173 K at 10 K/min, a recovery of their high mesoporous structural order was observed. After TPO, the maximum slopes of the inflection step for catalyst synthesized from HiSil and Cab-O-Sil became 2016 and 3099 while their fwhm of their PSDs also decreased to 3.73 Å and 2.84 Å, respectively. The recovery of mesoporosity of the Fe–MCM-41 (HiSil) demonstrates almost complete pore blockage after carbon deposition but not destruction of the pore structure.

Conclusions

There is an improvement in the structural order of siliceous MCM-41 upon the incorporation of 1 wt % Fe as a result of the knitting effect, but it diminishes as more Fe is incorporated. Catalysts synthesized from Cab-O-Sil showed higher structural order and higher stability during acetylene pyrolysis than catalysts synthesized from HiSil. Fe³⁺ species in all of the as-synthesized samples were found in the framework environment. Calcination causes the dislodgement of the Fe³⁺ species from

framework location and this effect is more severe for catalysts with ca. 2 and 3 wt % Fe. Fe³⁺ species occupying tetrahedral coordination decreases with increasing Fe loading.

This work reveals that Fe–MCM-41 (2 wt %) exhibits high selectivity for CNTs production under our optimized conditions (1073 K, 200 cm³/g-min C₂H₂/N₂, reaction duration of 1 h). Bundles or individual SWNTs in large amounts are obtained. Fe–MCM-41 (3 wt %) exhibit much lower selectivity toward CNT production and those formed are MWNT. Fe–MCM-41 (1 wt %) is not selective for CNT production. The relationship between the amount of Fe incorporated in MCM-41 and the carbon species produced during acetylene pyrolysis has therefore been established. Compared to the CO disproportionation process over Co–MCM-41, the acetylene pyrolytic process over Fe–MCM-41 provides lower selectivity to a narrow tube size distribution but very high overall yield.

Spectroscopic studies (EPR) of the catalysts after reaction revealed that Fe³⁺ species in Fe–MCM-41 (1 wt %) remained mainly in the framework and this partly accounts for its poor selectivity for CNTs. Fe³⁺ species in Fe–MCM-41 (2 wt %) appears to be well distributed in both framework and extraframework environments. On the other hand, Fe³⁺ species in Fe–MCM-41 (3 wt %) are well reduced and exist mainly in extraframework locations.

Acknowledgment. This work was supported by DARPA-DSO and Office of Basic Energy Science, DOE. X-ray absorption beam time from NSLS Brookhaven National Laboratory is gratefully acknowledged. Thanks are also due to L. K. Lakshmi for technical support during EPR experiments.

References and Notes

- (1) (a) Kresge, C. T.; Leonowicz, M. G.; Roth, W. J.; Vartuli, J. C.; Beck, J. S. *Nature (London)* **1992**, 359, 710. (b) Beck, J. S.; Vartuli, J. C.; Roth, W. J.; Leonowicz, M. E.; Kresge, C. T.; Schmit, K. D.; Chu, C. T.-W.; Olson, D. H.; Sheppard, E. W.; McCullen, S. B.; Higgins, J. B.; Schlenker, J. L. *J. Am. Chem. Soc.* **1992**, 114, 10834.
- (2) Corma, A. *Chem. Rev.* **1997**, 97, 2373.
- (3) (a) Iijima, S. *Nature* **1991**, 354, 56. (b) Huczko, A. *Appl. Phys. A* **2002**, 74, 617.
- (4) Lim, S.; Ciuparu, D.; Pak, C.; Dobek, F.; Chen, Y.; Harding, D.; Pfefferle, L.; Haller, G. *J. Phys. Chem. B* **2003**, 107, 11048.
- (5) Ciuparu, D.; Chen, Y.; Lim, S.; Haller, G. L.; Pfefferle, L. *J. Phys. Chem. B* **2004**, 108, 503.
- (6) (a) Li, Y.; Kim, W.; Zhang, Y.; Rolandi, M.; Wang, D.; Dai, H. *J. Phys. Chem. B* **2001**, 105, 11424. (b) Li, W. Z.; Xie, S. S.; Qian, L. X.; Chang, B. H.; Zou, B. S.; Zhou, W. Y.; Zhao, R. A.; Wang, G. *Science* **1996**, 274, 1701.
- (7) Hernadi, K.; Fonseca, A.; Nagy, J. B.; Bernaerts, D.; Lucas, A. A. *Carbon* **1996**, 34, 1249.
- (8) Hernadi, K.; Fonseca, A.; Nagy, J. B.; Siska, A.; Kiricsi, I. *Appl. Catal., A* **2000**, 199, 245.
- (9) Kong, J.; Cassele, A. M.; Dai, H. *Chem. Phys. Lett.* **1998**, 292, 567.
- (10) Rao, C. N. R.; Satishkumar, B. C.; Govindaraj, A.; Nath, M. *Chem. Phys. Chem.* **2001**, 2, 78.
- (11) Pérez-Cabero, M.; Rodríguez-Ramos, I.; Guerrero-Ruiz, A. *J. Catal.* **2003**, 215, 305.
- (12) Duxiao, J.; Nongyue, H.; Yuanying, Z.; Chunxiang, X.; Chunwei, Y.; Zuhong, L. *Mater. Chem. Phys.* **2001**, 69, 246.
- (13) Willems, I.; Kónya, Z.; Colomer, J.-F.; Van Tendeloo, G.; Nagaraju, N.; Fonseca, A.; Nagy, J. B. *Chem. Phys. Lett.* **2000**, 317, 71.
- (14) Kulovecz, A.; Kónya, Z.; Nagaraju, N.; Willems, I.; Tamási, A.; Fonseca, A.; Nagy, J. B.; Kiricsi, I. *Phys. Chem. Chem. Phys.* **2000**, 2, 3071.
- (15) Müller, T. E.; Reid, D. G.; Hsu, W. K.; Hare, J. P.; Kroto, H. W.; Walton, D. R. M. *Carbon* **1997**, 35, 951.
- (16) Huang, L.; Wind, S. J.; O'Brien, S. P. *Nano Lett.* **2003**, 3, 299.
- (17) Coquay, P.; Vandenberghe, R. E.; De Grave, E.; Fonseca, A.; Piedigrosso, P.; Nagy, J. B. *J. Appl. Phys.* **2002**, 92, 1286.
- (18) Ivanov, V.; Fonseca, A.; Nagy, J. B.; Lucas, A.; Lambin, P.; Bernaerts, D.; Zhang, X. B. *Carbon* **1995**, 33, 1727.
- (19) Lim, S.; Haller, G. L. *J. Phys. Chem. B* **2002**, 106, 8437.

- (20) Barrett, E. P.; Joyner, L. G.; Halenda, P. P. *J. Am. Chem. Soc.* **1951**, *73*, 373.
- (21) Lakshmi, K. V.; Eaton, S. S.; Eaton, G. R.; Frank, H. A.; Brudvig, G. W. *J. Phys. Chem. B* **1998**, *102*, 8327.
- (22) Ratnasamy, P.; Kumar, R. *Catal. Today* **1991**, *9*, 329.
- (23) Wang, Y.; Zhang, Q.; Shishido, T.; Takehira, K. *J. Catal.* **2002**, *209*, 186.
- (24) Gregg, S. J.; Sing, K. S. W. *Adsorption, Surface Area and Porosity*; Academic Press Inc.: London, 1982.
- (25) Yang, Y.; Lim, S.; Wang, C.; Harding, D.; Haller, G. *Microporous Mesoporous Mater.* **2004**, *67*, 245.
- (26) Echchahed, B.; Moen, A.; Nicholson, D.; Bonneviot, L. *Chem. Mater.* **1997**, *9*, 1716.
- (27) Bordiga, S.; Buzzoni, R.; Geobaldo, F.; Lamberti, C.; Giamello, E.; Zecchina, A.; Leofanti, G.; Petrini, G.; Tozzola, G.; Vlaic, G. *J. Catal.* **1996**, *158*, 486.
- (28) Samanta, S.; Giri, S.; Sastry, P. U.; Mal, N. K.; Manna, A.; Bhaumik, A. *Ind. Eng. Chem. Res.* **2003**, *42*, 3012.
- (29) Tuel, A.; Arcon, I.; Millet, J. M. M. *J. Chem. Soc., Faraday Trans.* **1998**, *94*, 3501.
- (30) Berlier, G.; Spoto, G.; Fisticaro, P.; Bordiga, S.; Zecchina, A.; Giamello, E.; Lamberti, C. *Microchem. J.* **2002**, *71*, 101.
- (31) Goldfarb, D.; Bernardo, M.; Strohmaier, K. G.; Vaughan, D. E. W.; Thomann, H. *J. Am. Chem. Soc.* **1994**, *116*, 6344.
- (32) Stockenhuber, M.; Hudson, M. J.; Joyner, R. W. *J. Phys. Chem. B* **2000**, *104*, 3370.
- (33) Berry, A.; O'Neill, H. C.; Jayasuriya, K. D.; Campbell, S. J.; Foran, G. *J. Am. Miner.* **2003**, *88*, 967.
- (34) Lin, H.-Y.; Chen, Y.-W.; Li, C. *Thermochim. Acta* **2003**, *400*, 61.
- (35) Lim, S.; Ciuparu, D.; Chen, Y.; Pfefferle, L.; Haller, G. L. *Top. Catal.* (In Press).
- (36) (a) Liu, B. C.; Lyu, S. C.; Jung, S. I.; Kang, H. K.; Yang, C.-W.; Park, J. W.; Park, C. Y.; Lee, C. J. *Chem. Phys. Lett.* **2004**, *383*, 104. (b) Ci, L.; Xie, S.; Tang, D.; Yan, X.; Li, Y.; Liu, Z.; Zou, X.; Zhou, W.; Wang, G. *Chem. Phys. Lett.* **2001**, *349*, 191. (c) Bladh, K.; Falk, L. K. L.; Rohmund, F. *Appl. Phys. A* **2000**, *70*, 317.
- (37) Lim, S.; Ciuparu, D.; Chen, Y.; Yang, Y.; Pfefferle, L.; Haller, G. L. *J. Phys. Chem. B* **2004**, ASAP DOI: 10.1021/jp048881(+).
- (38) Ciuparu, D.; Chen, Y.; Lim, S.; Yang, Y.; Haller, G. L.; Pfefferle, L. *J. Phys. Chem. B* **2004**, *108*, 15565.
- (39) Bandow, S.; Asaka, S.; Saito, Y.; Rao, A. M.; Grigorian, L.; Richter, E.; Eklund, P. C. *Phys. Rev. Lett.* **1998**, *80*, 3779.